Unifying principles of calcium wave propagation — insights from a three-dimensional model for atrial myocytes

R Thul
School of Mathematical Sciences
University of Nottingham
Nottingham, NG7 2RD

K Rietdorf and M D Bootman
Department of Life, Health and Chemical Sciences
The Open University, Walton Hall
Milton Keynes, MK7 6AA

S Coombes
School of Mathematical Sciences
University of Nottingham
Nottingham, NG7 2RD

Abstract

Atrial myocytes in a number of species lack transverse tubules. As a consequence the intracellular calcium signals occurring during each heart beat exhibit complex spatio-temporal dynamics. These calcium patterns arise from saltatory calcium waves that propagate via successive rounds of diffusion and calcium-induced calcium release. The many parameters that impinge on calcium-induced calcium release and calcium signal propagation make it difficult to know *a priori* whether calcium waves will successfully travel, or be extinguished. In this study, we describe in detail a mathematical model of calcium signalling that allows the effect of such parameters to be independently assessed. A key aspect of the model is to follow the triggering and evolution of calcium signals within a realistic three-dimensional cellular volume of an atrial myocyte, but with a low computational overhead. This is achieved by solving the linear transport equation for calcium analytically between calcium release events and by expressing the onset of calcium liberation as a threshold process. By being able to follow the evolution of a calcium wave in three dimensions, the model makes non-intuitive predictions about calcium signal propagation. For example, our modelling illustrates that the boundary of a cell produces a wave-guiding effect that enables calcium ions to propagate further and for longer, and can subtly alter the pattern of calcium wave movement. The high spatial resolution of the modelling framework allows the study of any arrangement of calcium release sites. We demonstrate that even small variations in randomly positioned release sites cause highly heterogeneous cellular responses.

Key words: calcium wave ; fire-diffuse-fire; computational cell biology; atrial myocyte; Green's functions

Introduction

All cell types use calcium (Ca^{2+}) as a messenger (1). However, the spatial and temporal characteristics of Ca^{2+} signals vary enormously between different tissues (2). The expression of diverse Ca^{2+} channels, pumps and buffers, coupled with particular cellular morphologies, underlies the cell-specific variations in Ca^{2+} signalling (3). For example, excitable cells express voltage-gated Ca^{2+} channels (VGCCs) that sense changes in membrane potential and rapidly gate the influx, or release, of Ca^{2+}. Consequently, Ca^{2+} signals in excitable cells can arise within tens of milliseconds, for example to trigger muscle contraction (4). Ca^{2+} signalling in non-excitable cells is often much slower. Typically, non-excitable cell types show repetitive Ca^{2+} oscillations that take several seconds to reach peak amplitude and tens of seconds to return to basal levels (5, 6). A well-known example is Ca^{2+} oscillations in glucagon-stimulated hepatocytes that regulate the release of glucose from glycogen (7). Despite substantial differences in the spatial and temporal properties of Ca^{2+} signals between various cell types, there are many similarities that allow direct mechanistic comparisons to be drawn. For example, the movement of Ca^{2+} within many cell types occurs in the form of saltatoric Ca^{2+} waves that reflect the sequential activation of clusters of Ca^{2+} release channels in a process known as Ca^{2+}-induced Ca^{2+} release (CICR) (8). Such saltatoric Ca^{2+} waves occur in cells as diverse as fully-differentiated atrial myocytes in the heart, and totipotent, fertilised oocytes (9, 10).

In the case of an atrial myocyte, incoming action potentials activate VGCCs to initially cause an increase of Ca^{2+} concentration just beneath the sarcolemma, around the periphery of the cell (11). This peripheral Ca^{2+} signal diffuses into the cell and triggers Ca^{2+} release from clusters of ryanodine receptors (RyRs) on the sarcoplasmic reticulum (SR), thereby amplifying the Ca^{2+} signal and allowing it to diffuse still further. Depending on prevailing conditions, repetitive rounds of diffusion and CICR lead to a centripetal Ca^{2+} wave that can fully engulf the interior of a myocyte (12).

For oocytes, fertilisation leads to the production of the intracellular messenger inositol 1,4,5-trisphosphate ($InsP_3$), which evokes Ca^{2+} release by binding to $InsP_3$ receptors ($InsP_3Rs$) on the surface of the endoplasmic reticulum (ER) (13). Although $InsP_3Rs$ require the binding of $InsP_3$ to facilitate their opening, they are activated by Ca^{2+} and can therefore participate in CICR responses in the same manner as RyRs (14). Production of $InsP_3$ therefore leads to saltatoric propagation of Ca^{2+} waves through sequential activation of clusters of $InsP_3Rs$ (15, 16). The two cell systems described above, atrial myocytes and oocytes, differ in the nature of their

Ca^{2+} release channels (RyRs versus $InsP_3Rs$), their internal calcium stores (SR versus ER), the arrangement of Ca^{2+} release sites (myocytes have a regular RyR array; oocytes have a random $InsP_3R$ distribution), frequency of Ca^{2+} signals and physiological significance of their Ca^{2+} increases. However, they both rely on saltatoric propagation of Ca^{2+} waves underpinned by rounds of CICR from clusters of Ca^{2+} channels, with the Ca^{2+} release sites being linked by cytoplasmic diffusion of Ca^{2+}. Given this similarity, it is possible to construct mathematical models of Ca^{2+} wave propagation that apply to either situation using the same basic features.

We recently developed a computational model that describes the propagation of Ca^{2+} signals during EC-coupling in atrial myocytes (17). The purpose of the model was to understand the centripetal propagation of Ca^{2+} signals from the cell periphery to cell centre. This centripetal propagation is necessary for triggering atrial myocyte contraction (18). The geometry of the modelling framework was based on the experimentally-determined regular lattice-like arrangement of RyR clusters within cardiac myocytes (19). The model successfully recapitulates known aspects of atrial myocyte excitation-contraction (EC) coupling and demonstrates how inotropic stimulation promotes centripetal Ca^{2+} wave propagation as a means of regulating contraction. Moreover, the model has a predictive capacity, and illustrates how sustained arrhythmic Ca^{2+} waves can be initiated by stochastic RyR activation (20). In the present study, we show that the model makes non-intuitive predictions about Ca^{2+} movement in atrial myocytes. In essence, the model highlights subtle, subcellular alterations in the propagation of Ca^{2+} signals depending on stimulation conditions and cellular status that are beyond the temporal and spatial sensitivity of current imaging technologies. Moreover, we describe in detail the model building process and outline the concomitant technical challenges and possible solutions. This can be used as a guideline to adapt the computational framework to other cell types with their specific cellular geometry and distribution of Ca^{2+} release sites. Overall, the modelling concept used here provides an ideal platform to study intracellular signalling pathways over time in three-dimensional cellular environments in a computationally non-expensive manner.

Materials and Methods

The dynamics of the cytosolic Ca^{2+} concentration $c(\mathbf{r}, t)$, $\mathbf{r} \in V \subset \mathbb{R}^3$, $t \in \mathbb{R}^+$, is governed by the equation $\mathcal{L}c(r, t) = I(r, t)$ with

$$\mathcal{L} = \frac{\partial}{\partial t} - D\Delta + \frac{1}{\tau} \,, \qquad I(\mathbf{r}, t) = \sum_{n \in \Gamma} \sum_{m \in \mathbb{N}} \delta\left(\mathbf{r} - \mathbf{r}_n\right) \eta\left(t - T_n^m\right) \,, \quad (1)$$

subject to boundary conditions of the form

$$a_1 \frac{\partial c}{\partial n} = a_2(c - a_3) \,, a_i \in \mathbb{R} \,. \tag{2}$$

We refer the reader to (6, 21–26) for a general discussion on modelling intracellular Ca^{2+}. In Eq. 1, D and Δ denote the effective diffusion coefficient for Ca^{2+} and the Laplace operator, respectively. We model the sarco-endoplasmic reticulum Ca^{2+} ATPase (SERCA) pumps as spatially homogeneous sinks of strength τ. A linear SERCA pump description corresponds to a low-affinity approximation of a biophysical model (27, 28). Linear SERCA pumps have been used successfully in the past for the mathematical analysis of travelling Ca^{2+} waves and three-dimensional numerical simulations of interacting Ca^{2+} release events (29–32). The current I corresponds to Ca^{2+} liberation from the SR through RyR channels. The N_{rel} release sites are located at discrete positions $\mathbf{r}_n$, $n \in \Gamma = \{1, \ldots, N_{\mathrm{rel}}\}$. The temporal shape of each release event is described by $\eta(t)$, which we here take as $\eta(t) = \sigma\Theta(t)\Theta\left(t - t_{\mathrm{rel}}\right)$. The Heaviside step function Θ, which equals 1 for $x \geq 0$ and 0 otherwise, restricts the duration of release events to t_{rel}, which corresponds to the typical life time of a Ca^{2+} release event. The release strength is assumed to be constant and is denoted by σ. The time T_n^m in Eq. 1 corresponds to the instant when the nth release site conducts Ca^{2+} for the mth time, which is defined by

$$T_n^m = \inf\left\{t \mid c(\mathbf{r}_n, t) > c_{\mathrm{th}}, \ t > T_n^{m-1} + t_{\mathrm{ref}}\right\} \,, \tag{3}$$

where we introduce the absolute refractory period t_{ref}. The computation of the release times T_n^m renders Eq. 1 highly nonlinear, because the mth liberation is obtained implicitly by demanding that the Ca^{2+} concentration reaches the threshold value c_{th} at time T_n^m and that there is at least a period of t_{ref} between successive release events.

We now assume that all release events occur at multiples of some dt. In this case we can rewrite Eq. 1 for $p\mathrm{d}t \leq t \leq (p+1)\mathrm{d}t$, $p \in \mathbb{N}$, as

$$\mathcal{L}c\left(\mathbf{r}, \mathbf{t}\right) = \sigma \sum_{n \in \Gamma} a_n(p)\delta\left(\mathbf{r} - \mathbf{r}_n\right) \,. \tag{4}$$

The indicator function $a_n(p)$ is a binary variable that takes on the value 1 when $T_n^m < t < T_n^m + t_{\text{rel}}$ and is 0 otherwise. Introducing the notation $c_p(\mathbf{r}) = c(\mathbf{r}, p\mathrm{d}t)$ and using Green's function theory (33), we find from Eq. 4

$$c_{p+1}(\mathbf{r}) = \sigma \sum_{n \in \Gamma} a_n(p) H(\mathbf{r}, \mathbf{r}_n, \mathrm{d}t) + I_p(\mathbf{r}), \tag{5}$$

with

$$H(\mathbf{r}, \mathbf{r}', t) = \int_0^t G(\mathbf{r}, \mathbf{r}', s)\,\mathrm{d}s, \qquad I_p(\mathbf{r}) = \int_V G(\mathbf{r}, \mathbf{r}', \mathrm{d}t)\,c_p(\mathbf{r}')\,\mathrm{d}\mathbf{r}', \tag{6}$$

where $G(\mathbf{r}, \mathbf{r}', t)$ is a modified Green's function of the operator $\mathcal{L}$ on the domain V. Instead of solving the Green's function for vanishing boundary conditions, we impose the same boundary conditions on G as we do for c. This results in the cancellation of the surface term usually present in Eq. 5. Note that for constant $\mathrm{d}t$ the basis functions $H(\mathbf{r}, \mathbf{r}', \mathrm{d}t)$ need to be computed only once. The specific form of G depends on the geometry of the problem at hand and the boundary conditions. As the model was originally designed for atrial myocytes, a cylindrical coordinate system (r, θ, z) is the most appropriate choice. Hence, $\mathcal{L}$ is given by

$$\mathcal{L} = \frac{\partial}{\partial t} + \frac{1}{\tau} - D\left(\frac{\partial^2}{\partial r^2} + \frac{1}{r}\frac{\partial}{\partial r} + \frac{1}{r^2}\frac{\partial^2}{\partial \theta^2} + \frac{\partial^2}{\partial z^2}\right). \tag{7}$$

We impose finite fluxes across the surface of the cylinder, which mimic e.g. plasma membrane pumps or Na^+/Ca^{2+} exchangers. This gives rise to the boundary conditions

$$\frac{\partial c}{\partial r} + hc = 0, \quad r = R, \tag{8}$$

where $\partial/\partial r$ is the outward radial derivative, and

$$\frac{\partial c}{\partial z} - h_0 c = 0, \quad z = 0, \qquad \frac{\partial c}{\partial z} + h_l c = 0, \quad z = l. \tag{9}$$

Subject to the same boundary conditions as c, the Green's function G can be written as

$$G(\mathbf{r}, \mathbf{r}', t) = \sum_\alpha P_\alpha(z, z') p_\alpha(t) \sum_{n=-\infty}^{\infty} \sum_\beta Q_{n,\beta}(r, \theta, r', \theta') q_\beta(t), \tag{10}$$

with

$$P_\alpha(z, z') = \frac{(\alpha \cos \alpha z + h_0 \sin \alpha z)(\alpha \cos \alpha z' + h_0 \sin \alpha z')}{l\left(\alpha^2 + h_0^2\right) + 2h_0} , \qquad (11a)$$

$$Q_{n,\beta}(r, \theta, r', \theta') = \frac{2 \cos n\left(\theta - \theta'\right)}{\pi a^2} \frac{\beta^2 \mathrm{J}_n\left(\beta r\right) \mathrm{J}_n\left(\beta r'\right)}{\left(h^2 + \beta^2 - n^2/a^2\right) \mathrm{J}_n^2\left(\beta a\right)} , \qquad (11b)$$

and $p_\alpha(t) = \exp[-(1/\tau + D\alpha^2)t]$, $q_\beta(t) = \exp[-D\beta^2 t]$. The eigenvalues α and β are determined implicitly by

$$\left(\alpha^2 - h_0 h_l\right) \tan(\alpha l) = \alpha\left(h_0 + h_l\right), \qquad \beta \mathrm{J}_n'\left(\beta a\right) + h \mathrm{J}_n\left(\beta a\right) = 0. \qquad (12)$$

Here, $J_n(x)$ denotes the Bessel function of the first kind of order n (34), and $J_n'(x)$ represents the first derivative with respect to x. Note that Eqs. 12 give rise to infinitely many eigenvalues, and that the value of β depends on the order of the Bessel function. For other idealised geometries it is also possible to calculate the Green's function using series expansions of special functions. Spherical cells using Green's functions have been studied in (30, 35). A key step in the computation of the Ca^{2+} concentration is the evaluation of the basis function $H\left(\mathbf{r}, \mathbf{r}_n, dt\right)$ given by Eq. 6. A computationally fast scheme for this evaluation, using re-summation techniques for convergence acceleration, is described in Appendix A.

To mimic the effect of channel noise (36–41) we further consider a fluctuating threshold given by the replacement $c_{th} \rightarrow c_{th} + \xi$ (42). Here, ξ is a random variable with a mean of zero and cumulative probability function

$$F_\xi(x) = \left[\frac{1}{1 + e^{-\beta x}} - \frac{1}{1 + e^{\beta c_{th}}}\right]\left(1 + e^{-\beta c_{th}}\right), \qquad (13)$$

i.e. $\mathrm{Prob}(\xi < x) = F_\xi(x)$. In contrast to the deterministic case when a release site that is not refractory at position $\mathbf{r}_n$ starts liberating Ca^{2+} as soon as $c(\mathbf{r}_n, t) > c_{th}$ each site now has a probability for $c(\mathbf{r}_n, t) > c_{th} + \xi$. This probability is given by $\mathrm{Prob}(c(\mathbf{r}_n, t) > c_{th} + \xi) = \mathrm{Prob}(\xi < c(\mathbf{r}_n, t) - c_{th}) = F_\xi(c(\mathbf{r}_n, t) - c_{th})$. We incorporate the stochastic Ca^{2+} release in the above framework by making $a_n(p)$ a binary random variable that takes on the value 1 with probability $F_\xi(c_p(\mathbf{r}_n) - c_{th})$. The probability of release approaches zero for small Ca^{2+} concentrations and tends to one as c becomes large. The strength of the fluctuations is controlled by β, such that larger values of β correspond to a smaller threshold noise strength. In the limit $\beta \rightarrow \infty$, the probability $F_\xi\left(c - c_{th}\right)$ reduces to the step function $\Theta(c - c_{th})$ and we recover the deterministic release model. Table 1 lists the standard set of

parameter values used in the simulations. Diffusion of Ca^{2+} is captured by an effective diffusion coefficient incorporating the effect of buffers on Ca^{2+} diffusion. A release strength of 15 μM μm^3/s corresponds to approximately 23 Ca^{2+} liberating channels (43, 44). If no value for β is noted in the figure caption the simulations are deterministic.

In recent years, the impact of models on designing and explaining cellular experiments has increased significantly (see e.g. (45)). For many models, exploring the effects of different stimulus conditions often requires scanning large areas of parameter space. For detailed cell signalling models such scans become very quickly computationally demanding, if not prohibitive. Our computational framework is ideally suited to reduce such computational costs. One main advantage of our approach is that the Green's function, G, and the time integral, H, need to be computed only once for scanning e.g. the influence of release strength, release duration, refractory periods or stimulation protocols on Ca^{2+} wave propagation. The main computational overhead then arises from the summation of the contribution of all active Ca^{2+} release sites to the cellular Ca^{2+} signal (Eq. 5). However, this step is amenable to parallelisation, which reduces computational costs significantly. A particular advantage of a cylindrical geometry is the product structure of the Green's function (Eq. 10). The longitudinal contribution (z coordinate) formally separates from the polar coordinates (r and θ). Let N_z, N_r and N_θ denote the number of points for the spatial discretisation in the z, r and θ direction, respectively. The product structure of Eq. 10 entails that we only need to compute $(N_z + (N_r \times N_\theta))^2$ terms for a given pair of eigenvalues α and β instead of $(N_z \times N_r \times N_\theta)^2$ — the square results from taking into account both unprimed and primed coordinates. This constitutes a massive saving in the memory costs associated with the Green's function and allows us to work at high spatial resolution. The product structure of the Green's function also entails that sometimes only parts of the Green's function have to be recomputed, while other terms remain unaffected. For example, this is the case for studying the impact of SERCA pumps. The strength of the SERCA pumps enters through p_α, which only affects the longitudinal contribution of the Green's function, but not the polar terms.

Results and Discussion

Rationale for a three-dimensional atrial myocyte model

A key aim of the present study was to explore the utility of our modelling concept for monitoring calcium signal propagation in three-dimensional space,

and with high spatial and temporal resolutions. In particular, we sought to examine how modest changes in Ca^{2+} transport, or in the triggering of Ca^{2+} signals, alters the propagation of Ca^{2+} signals. A detailed description of the equations used is given in the Materials and Methods section. In essence, we modelled an atrial myocyte as a cylinder with a regular lattice-like array of Ca^{2+} release sites that are positioned on 51 z-disks (akin to the z-lines seen in transverse sections of an atrial myocyte; (11)). Figures 1Ai–iv illustrate the basic cylindrical shape of acutely-isolated atrial myocytes, despite some variability in the shape of individual cells. Each z-disk has 100 discrete Ca^{2+} release sites arranged in concentric rings (Fig. 1B). Within the modelling framework, Ca^{2+} signals can be triggered by the immediate activation of Ca^{2+} release sites anywhere within the volume of the cell. Propagation of the resultant Ca^{2+} signal relies on the diffusion of Ca^{2+} ions between sites. If sufficient Ca^{2+} ions diffuse from a triggered site to its neighbouring sites then CICR will occur, and the Ca^{2+} signal will propagate further. The variables determining the threshold for triggering CICR, Ca^{2+} release flux strength and refractoriness at each site can be independently altered. The propagation of Ca^{2+} signals within a z-disk is hindered by the action of Ca^{2+} pumps and diffusion of Ca^{2+} ions out of the z-disk and into the 3-dimensional volume of the myocyte. It is important to note that the diffusion of Ca^{2+} between z-disks can trigger longitudinal Ca^{2+} waves via CICR. The model can therefore resolve Ca^{2+} wave propagation both within and between z-disks (20).
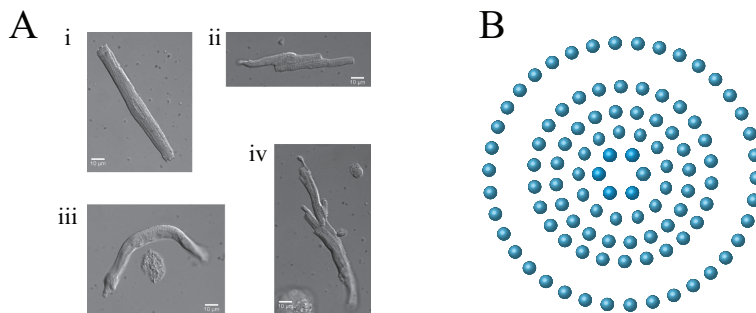

Figure 1: (A) Representative bright-field images of acutely-isolated atrial myocytes illustrating the variation in shape between individual cells. (B) Position of Ca^{2+} release sites within a single z-disk as used in the simulations.

Although atrial myocytes in some species express transverse tubules (46, 47), the model is based on our prior experiments using rat myocytes that

largely do not possess invaginations of the sarcolemma (48). Depolarisation of the atrial myocyte sarcolemma therefore activates VGCCs around the cellular periphery, and initially causes a sub-sarcolemmal Ca^{2+} rise (10, 18). If this sub-sarcolemmal Ca^{2+} signal does not propagate inwards atrial myocytes display only a modest contraction. However, under conditions favouring positive inotropy (e.g. greater SR Ca^{2+} release flux or lower threshold for CICR) the sub-sarcolemmal Ca^{2+} signal triggers a centripetal Ca^{2+} wave that propagates to the myocyte interior. The extent of centripetal propagation determines the magnitude of myocyte contraction (18). Essentially, as the Ca^{2+} wave spreads it engages an increasing number of myofilaments (11). A particular structural aspect of atrial myocytes that impacts on Ca^{2+} signal development is a gap in the expression of RyRs between those at the periphery and those towards the centre of the cell (11, 49). Such a gap in RyR expression has been universally observed in atrial myocytes from different species (11, 49). Atrial myocytes can therefore be considered to express two populations of RyRs. The junctional RyRs sit beneath the sarcolemma, and are responsible for the initiation of Ca^{2+} signals during EC-coupling. In contrast, non-junctional RyRs are expressed on the other side of a $\sim 2~\mu m$ gap. The non-junctional RyRs participate in the passage of a centripetal wave via CICR if an activating Ca^{2+} signal arises at the junctional RyRs and successfully crosses the gap.

It is possible to discretely trigger any of the 5100 Ca^{2+} release sites within the volume of the model. By acutely activating the junctional, peripheral, Ca^{2+} release sites (or a subset thereof), the model recapitulates EC-coupling in atrial myocytes. Alternatively, activating sites deep within an atrial myocyte would generate a Ca^{2+} trigger akin to spontaneous, pathological, activation of RyRs. Within an atrial myocyte, spontaneous Ca^{2+} release events can cause electrical events, such as delayed afterdepolarisations, if they reach the sarcolemma and activate electrogenic transporters. Following an initial activation, the model then determines the evolution of the resultant Ca^{2+} signal. Examples of Ca^{2+} wave propagation within a z-disk are depicted in Fig. 2. Ca^{2+} signals were initiated by activation of peripheral Ca^{2+} release sites, as they would be during atrial myocyte EC-coupling. In Fig. 3Ai, 90% of the peripheral Ca^{2+} release sites were triggered, thereby giving rise to an almost completely circular Ca^{2+} wave that moved centripetally into the z-disk (Fig. 2Aii and iii). For Figs. 3 Bi and Ci, 60% and 40%, respectively, of the peripheral release sites were initially triggered. These weaker initial stimuli did not give rise to circular Ca^{2+} waves. Rather, they evoked asymmetric Ca^{2+} waves that had heterogeneous patterns and limited centripetal propagation (Figs. 2Bii – iii and 2Cii – iii). These data illustrate the ability

of the modelling framework to predict the detailed movement of Ca^{2+} signal under varying conditions. By stacking z-disks vertically, the model can easily transition from a single two-dimensional plane to a three-dimensional volume, but still allowing the same spatial and temporal resolution in each z-disk. Although Fig. 2 depicts Ca^{2+} wave movement for a single z-disk, Ca^{2+} signals can be simultaneously monitored for any, or all, of the other z-disks. We have previously shown that our simulation recapitulates the faster and more extensive centripetal Ca^{2+} waves seen under inotropic stimulation of atrial cells (17). In addition, the model demonstrates the evolution of self-sustaining Ca^{2+} waves that progressively dominate electrical pacing of atrial cells (20). Moreover, our simulations have shown that the gap in RyR expression acts as a diffusion barrier to the movement of Ca^{2+}, and constrains atrial contraction under resting conditions (17).

The sarcolemma acts as a 'wave guide' to enhance Ca^{2+} transport

While performing these prior studies, we observed that modifying stimulation or Ca^{2+} release parameters could have profound, non-intuitive effects on the propagation of Ca^{2+} signals within an atrial myocyte. This applies to the propagation of both subcellular and global Ca^{2+} signals. An example is depicted in Fig. 3, which shows spatially-resolved snapshots of two travelling Ca^{2+} waves. For both Ca^{2+} waves, the initial trigger was the same (simultaneous activation of 6 Ca^{2+} release sites coloured red at one edge of the central z-disk). However, the Ca^{2+} waves propagate quite differently both within the initiating z-disk, and between neighbouring z-disks. The only parameter altered in these two situations was the Ca^{2+} flux magnitude (denoted in the model as 'release strength'; σ) at every Ca^{2+} release site. In the left-hand panels (Figs. 3Ai – iii), the release strength was 140 μM μm^3/s. In this situation, the Ca^{2+} wave propagated rapidly around the circumference of the initiating z-disk, with the sarcolemmal boundary acting as a wave guide. Eventually, the circumferential Ca^{2+} wave evoked both a centripetal Ca^{2+} wave within the central z-disk, and longitudinal Ca^{2+} waves that moved to the top and bottom of the cell. With a lesser release strength ($\sigma = 20$ μM μm^3/s; Figs. 3Bi – iii), the initial Ca^{2+} signal did not trigger the circumferential and centripetal propagation of a Ca^{2+} wave, but rather a Ca^{2+} wave that simply propagated through the middle of the cell with an almost planar wave front. The lesser release strength also triggered longitudinal Ca^{2+} waves that moved through the z-disks of the cell (Figs. 3Bi – iii). However, the recruitment of Ca^{2+} release sites within each of the z-disks was spatially and temporally different to that seen with the higher release
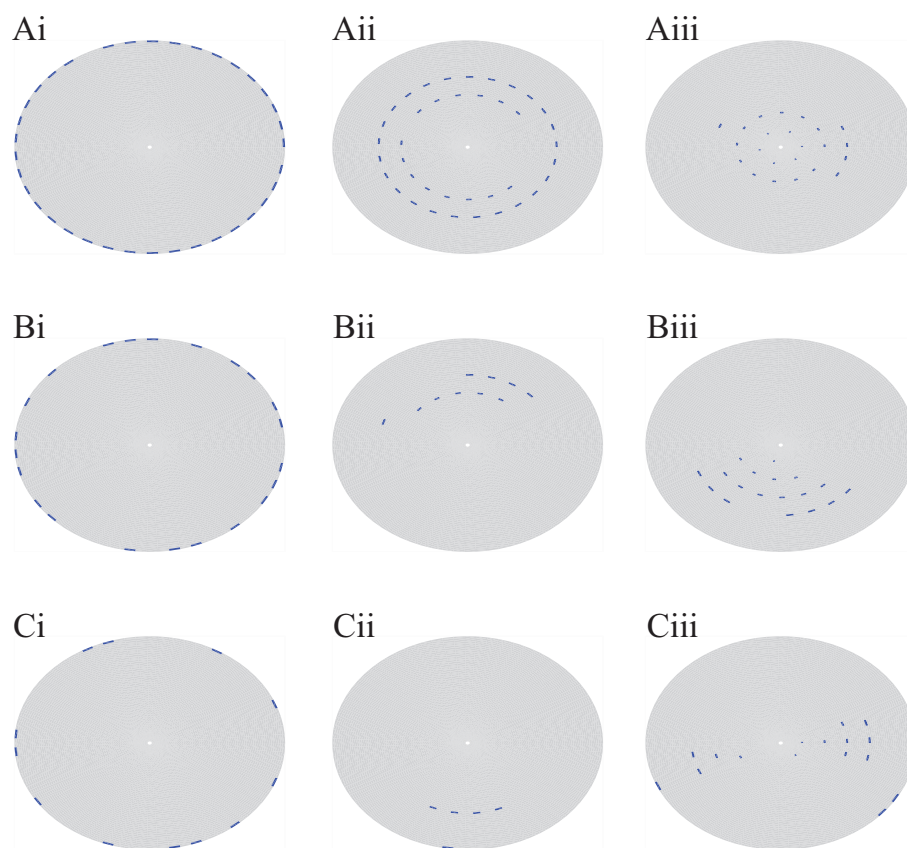
Ai   Aii   Aiii

Bi   Bii   Biii

Ci   Cii   Ciii

Figure 2: Travelling Ca^{2+} waves within a single z-disk for (A) initial fraction 0.9 at 0.03 s (i), 0.12 s (ii), 0.18 s (iii), (B) initial fraction 0.6 at 0.03 s (i), 0.20 s (ii), 0.33 s (iii), and (C) initial fraction 0.4 at 0.03 s (i), 0.27 s (ii), 0.38 s (iii). Activate Ca^{2+} release sites are shown in blue. Parameter values as in Table 1 and $\tau = 0.3$ s, $\sigma = 3.5$ μM μm^3/s, $t_{\text{ref}} = 1.3$ s.

strength.

These distinctive patterns of Ca^{2+} wave propagation emanate from the same cellular geometry and initial trigger, and arise simply due to a change of Ca^{2+} release strength. With a higher Ca^{2+} release strength, the circumferential movement of Ca^{2+} around the junctional RyRs proceeds much more quickly than diffusion of Ca^{2+} across the gap in RyR expression. The complete circumferential engagement of the junctional RyRs means that the ensuing centripetal Ca^{2+} wave is almost perfectly concentric. Whereas, with a lesser Ca^{2+} release strength, the relative difference in speed between circumferential and centripetal Ca^{2+} movement decreases, and the ensuing Ca^{2+} wave propagates as a planar wave across a z-disk.

By comparing the time stamps of the different panels in Fig. 3, we noted that the longitudinal Ca^{2+} wave travelled more quickly at higher Ca^{2+} release strength than at the smaller release strength. The Ca^{2+} wave reached the z-disks at $z = 25~\mu$m and $z = 75~\mu$m at 0.3 s in Fig. 3Aii, as compared to 0.48 s in Fig. 3Bii. The faster rate of Ca^{2+} wave propagation is an expected consequence of Ca^{2+} signal propagation via CICR. The higher the Ca^{2+} release strength, the larger the Ca^{2+} gradient around a Ca^{2+}-liberating release site. In turn, this gives rise to faster diffusion of Ca^{2+} from a liberating Ca^{2+} release site to an adjacent quiescent Ca^{2+} release site. Lowering the value of the release strength σ eventually leads to a situation where Ca^{2+} wave propagation is not supported within or between z-disks. Interestingly, σ values that lead to failed Ca^{2+} wave propagation within a z-disk also abolish longitudinal Ca^{2+} waves. This suggests that the initiation of a longitudinal Ca^{2+} wave first requires co-ordinated Ca^{2+} liberation within a z-disk. We suggest that co-ordinated Ca^{2+} liberation within a z-disk is needed to have a sufficient amount of Ca^{2+} diffusing from one plane to another to trigger CICR in a longitudinal direction. Movies S1 and S2 in the Supporting Material provide a detailed view on the 3-dimensional travelling Ca^{2+} waves following activation of Ca^{2+} release in one z-disk only.

A key feature in determining the different patterns of Ca^{2+} wave movement shown in Fig. 3 was the sarcolemmal membrane acting as a wave guide. This happens when the rate of Ca^{2+} release at a sub-sarcolemmal site exceeds the rate of Ca^{2+} extrusion across the sarcolemma. Consequently, Ca^{2+} ions are constrained to remain in the cell volume by the sarcolemmal barrier, and more prominently diffuse to neighbouring release sites. A further example of the significance of sarcolemmal wave guiding is illustrated in Fig. 4. The panels within Figs. 4A – C show the activity of all the 5100 Ca^{2+} release sites within the volume of the model. For ease of viewing, the model has been transformed into a 2-dimensional plot. At rest, all the Ca^{2+}
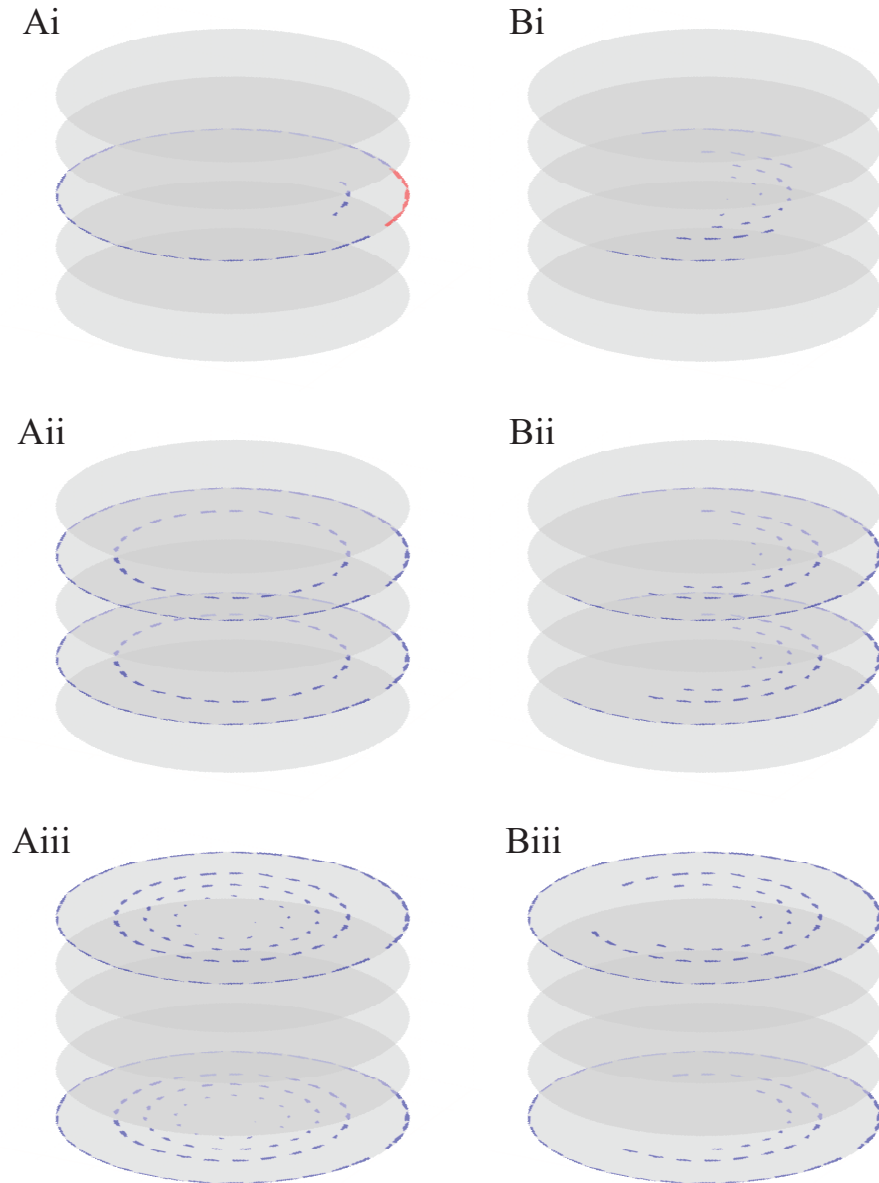
Figure 3: Travelling Ca^{2+} waves for $\sigma = 140$ μM μm^3/s (A) at 0.03 s (i), 0.30 s (ii), 0.59 s (iii) and $\sigma = 20$ μM μm^3/s (B) at 0.11 s (i), 0.48 s (ii), 0.85 s (iii). Active Ca^{2+} release sites are shown in red and blue. Waves were initiated by elevating the Ca^{2+} concentration at the release sites shown in red in Ai. Parameter values as in Table 1. The representative z-disks are located at $z = 1$, 24, 50, 76, 99 μm.
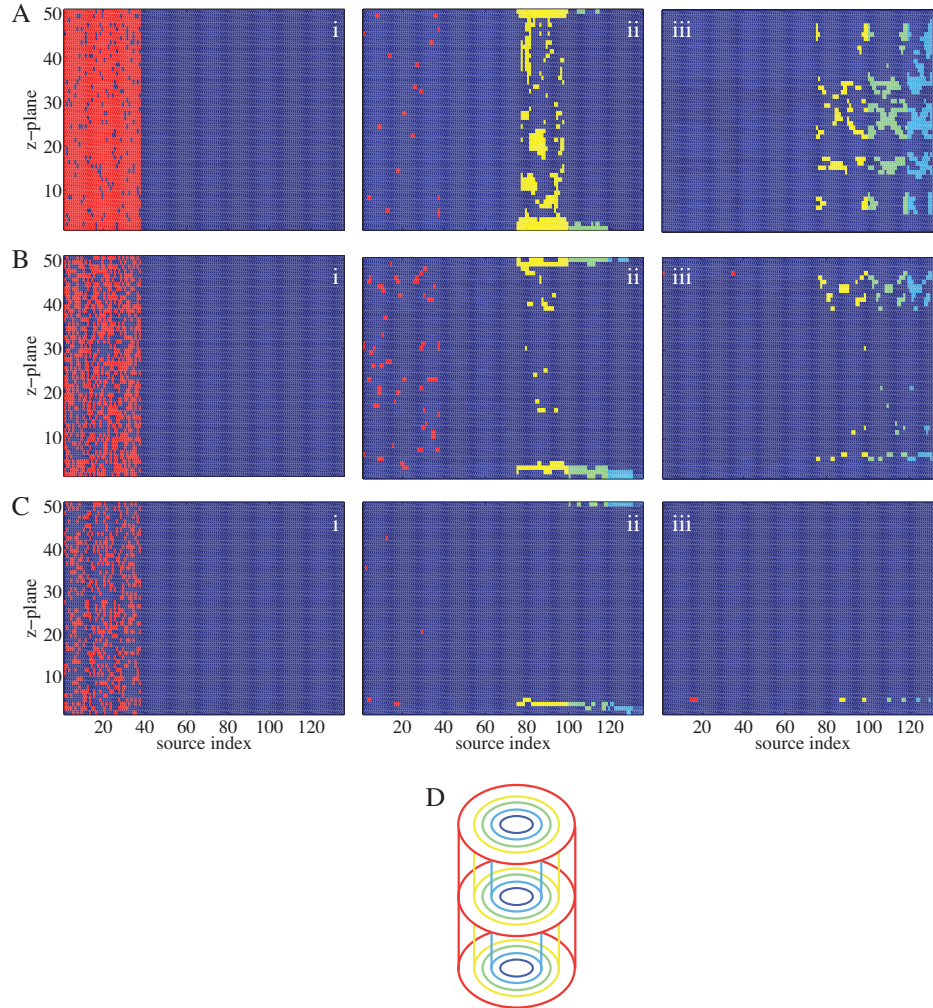
14

Figure 4: Time evolution of Ca^{2+} release activity at each Ca^{2+} release site within the model for different initial fractions of stimulated junctional Ca^{2+} release sites: 0.9 (A), 0.5 (B), 0.3 (C). Time points are 0.01 s (i), 0.15 s (ii) and 0.26 s (iii) in (A), 0.01 s (i), 0.15 s (ii) and 0.3 s (iii) in (B), 0.01 s (i), 0.21 s (ii) and 0.33 s (iii) in (C). Active Ca^{2+} release sites are shown in red, yellow, green, dark blue and medium blue. The colours in (A) – (C) indicate the radial position of Ca^{2+} release sites as shown in (D). See text for details. Parameter values as in Table 1 and $\tau = 0.3$ s, $t_{ref} = 1.3$ s, $\sigma = 3.5\mu M\ \mu m^3/s$.

release sites are inactive, which is indicated by dark blue pixels. When a Ca^{2+} release site becomes active it is assigned a different colour. The particular colour depends on where the Ca^{2+} release sites are located within the model. The outermost Ca^{2+} release sites are coloured red when they are activated, the next inner Ca^{2+} release sites are coloured yellow when they are activated, and the sequence then follows with green, light blue and medium blue pixels, as depicted by the coloured rings in the cartoon in Fig. 4D. The y-axis shows the vertical location of the 51 z-disks in the model, and the x-axis (source index) shows the position of Ca^{2+} release sites within a z-disk. For example, source indices 1 to 38 represent the Ca^{2+} release sites around the periphery of the cell. A centripetal Ca^{2+} wave would be identified by the successive activation of Ca^{2+} release sites starting at the periphery (red) and then moving rightwards with the colour sequence yellow, green, light blue and medium blue. Three different stimulation conditions are illustrated in Fig. 4. Figures 4Ai – iii depict the response that ensues when 90% of the junctional Ca^{2+} release sites are activated at the onset of stimulation. The activation of these peripheral Ca^{2+} release sites yields the bright red band shown in Fig. 4Ai. Subsequently, the Ca^{2+} signal moves centripetally and recruits Ca^{2+} release sites deeper within the cell. This Ca^{2+} wave could be considered to be largely successful in that a significant proportion of Ca^{2+} release sites within the innermost ring respond (medium blue pixels), and consequently the cell would be expected to have a large contractile response (18). For Figs. 4Bi – iii, the fraction of junctional Ca^{2+} release sites activated at the onset of the response was reduced to 50%. As a consequence, the Ca^{2+} wave propagated weakly into the cell interior. In contrast, activating only 30% of the junctional Ca^{2+} release sites (Figs. 4Ci – iii) did not evoke a centripetal Ca^{2+} wave in the central volume of the cell because the initial Ca^{2+} signal was not able to traverse the gap in RyR expression. In each of the situations shown in Fig. 4, whether or not there was a centripetal Ca^{2+} wave, it is evident that the Ca^{2+} signal propagated most rapidly and prominently along the top and bottom of the cell. This was due to the sarcolemma at the poles of the cell acting as a wave guide. The sarcolemmal boundary helps Ca^{2+} signals to propagate substantial distances and thereby limiting the loss of Ca^{2+} from the cellular volume. The wave guiding effect was evident with each condition, but was particularly evident with relatively weak stimulation (Figs. 4Ci – iii).

The ability of the sarcolemmal boundaries at the top and the bottom of the cell to act as wave guides has a significant effect on the kinetics and longevity of Ca^{2+} signals. This is illustrated in Fig. 5, where we plotted the number of active Ca^{2+} release sites within the cellular regions depicted

in Fig. 4 on a temporal scale. We used the same colour coding for the junctional (red lines in Fig. 5) and non-junctional (yellow, green, light blue, medium blue lines in Fig. 5) Ca^{2+} release sites. Figure 5A corresponds to the situation where 90% of the peripheral Ca^{2+} release sites were activated at the start of stimulation (c.f. Fig. 4A). In this case, the successful centripetal movement of Ca^{2+} is evident; the Ca^{2+} signal propagates towards the central regions of the cell albeit with a progressive delay, decline in upstroke and decrease in amplitude. The Ca^{2+} signal is fully terminated by ~ 0.35 s. Such a coordinated, transient, Ca^{2+} elevation represents an ideal EC-coupling event.
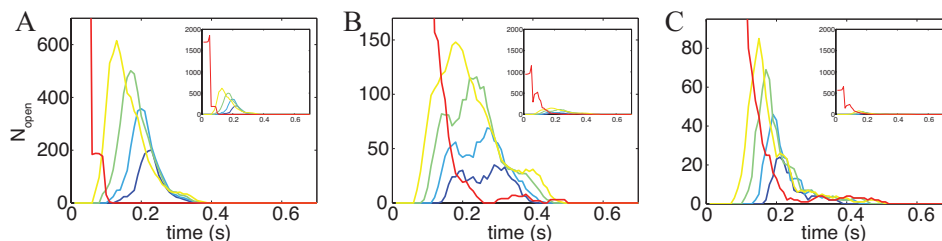

Figure 5: Temporal activation of Ca^{2+} release sites within the myocyte model. The three panels show Ca^{2+} signals arising from the different initial stimulus in Fig. 4. The y-axis shows the number of active Ca^{2+} release sites, Nopen, within particular regions of the model. The colours correspond to the positions of Ca^{2+} release sites depicted in Fig. 4 (i.e. red indicates peripheral Ca^{2+} release sites, whilst medium blue indicates the innermost ring of Ca^{2+} release sites). Insets show the data plotted for the same y-axis range.

In contrast, the situations depicted in Figs. 4B and 4C, where the sarcolemma behaved as a prominent wave guide gave different kinetic profiles. Specifically, the Ca^{2+} signal was found to persist within the central regions of the cell. This prolongation of the Ca^{2+} signal is evident when 50% (Fig. 5B) or 30% (Fig. 5C) of the peripheral Ca^{2+} release sites were initially stimulated. In these latter cases, the movement of Ca^{2+} along the top and bottom of the cell guides the Ca^{2+} signal towards quiescent Ca^{2+} release sites within the cell's central zones. Once there, the Ca^{2+} signal triggers CICR producing local, non-synchronous Ca^{2+} release events that persist for a while before gradually dwindling. The key finding here is that the wave guide effect of the sarcolemma overcomes the gap in RyR expression and allows the Ca^{2+} signal to travel further than it otherwise would.

The relatively slow, low-amplitude movement of the Ca^{2+} signal along the sarcolemmal boundary means that the subsequent CICR beyond the gap in RyR expression is poorly coordinated. The lack of coordination means that the RyRs do not go through synchronous activation and refractory periods, and therefore the Ca^{2+} signal can keep meandering within the central regions.

The analysis described above indicates that the sarcolemma can act as a wave guide and promote the long-distance diffusion of Ca^{2+} signals. If such wave guiding were to occur within atrial myocytes on a beat-to-beat basis, the cells would be prone to uncontrolled subcellular Ca^{2+} signals that are believed to serve as a basis for pro-arrhythmic activity. While atrial myocytes posses a basic cylindrical shape, there is some variability amongst them (Fig. 1). Those cells having a cuboidal shape (akin to the model) may be relatively more prone to the effects of sarcolemmal wave guiding, whereas cells with tapered poles could largely avoid these effects. The influence of atrial myocyte shape on Ca^{2+} diffusion has not been examined, to our knowledge. Nevertheless, wave guiding is an inevitable outcome of having a sarcolemmal boundary that hinders Ca^{2+} signal dissipation. Such wave guiding can affect subcellular properties of Ca^{2+} waves (Fig. 3) and promote the movement of Ca^{2+} ions over long distances (Figs. 4 and 5).

The impact of sarcolemmal and SR Ca^{2+} transport on EC-coupling

The influence of the sarcolemma on the evolution of Ca^{2+} signals depends on the rate of Ca^{2+} extrusion from the cell. We therefore explored the effect of sarcolemmal Ca^{2+} extrusion on the development of Ca^{2+} signals during EC-coupling in more detail. To do this, we examined the relative success of activating central Ca^{2+} release sites in situations where the sarcolemmal Ca^{2+} flux rate was altered (Fig. 6A; sarcolemmal Ca^{2+} transport is implemented as 'boundary flux' in the model). Centripetal Ca^{2+} waves were triggered by activating a fraction (from 0.2 to 1) of the peripheral Ca^{2+} release sites, and we monitored the proportion of central Ca^{2+} release sites that were subsequently recruited. The recruitment of central Ca^{2+} release sites was taken as a measure of successful centripetal Ca^{2+} waves that propagated to the cell interior, and by association Ca^{2+} signals that would trigger substantial contraction of an atrial myocyte. To obtain the data presented in Fig. 6, simulations were run multiple times with responses initiated by triggering different fractions of the peripheral Ca^{2+} release sites. With each simulation, the activated peripheral Ca^{2+} release sites were randomly selected so that data were not biased by particular configurations at
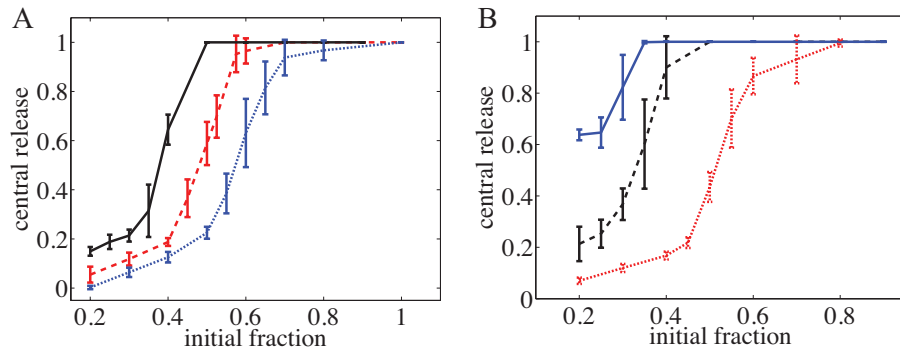
Figure 6: Activation of central Ca^{2+} release sites within the myocyte model as a measure of centripetal Ca^{2+} wave propagation. The data points in each panel show the mean relative response and standard deviation (error bars) of the central Ca^{2+} release sites (r = 0.9 μm) as a function of initial fraction for varying boundary fluxes (A) and different SERCA pump strengths (B). In (A) the boundary flux constants h, h_0 and h_l are given by 0.01 (black solid), 0.05 (red dashed), and 0.08 μm^{-1} (blue dotted), while the different colours in (B) correspond to $\tau = 0.7$ (blue solid), 0.5 (black dashed), and 0.3 s (red dotted). Parameter values as in Table 1, $t_{ref} = 1.3$ s, $\sigma = 3.5\mu M$ μm^3/s and $\tau = 0.5$ s.

the initiation of Ca^{2+} responses. The data points in Fig. 6 represent the relative mean of Ca^{2+} release sites activated within the innermost ring of Ca^{2+} release sites (+/- standard deviation). It might be expected that in deterministic models, such as that presented here, the propagation of Ca^{2+} signals would be entirely stereotypical from simulation to simulation. However, the wide error bars indicate that responses can be far from stereotypical. In fact, the wide error bars indicate that there are some configurations for the initial fraction of Ca^{2+} release sites that are less successful at generating centripetal Ca^{2+} waves than others. We have explored this point also in previous work (17). The black line in Fig. 6A illustrates that with relatively weak sarcolemmal Ca^{2+} transport, 100% recruitment of the central Ca^{2+} release sites could be achieved by activating only 50% of the peripheral Ca^{2+} release sites. However, if sarcolemmal Ca^{2+} transport was increased 5-fold (red line in Fig. 6A) or 8-fold (blue line in Fig. 6A), recruitment of central Ca^{2+} release required the activation of a greater fraction of peripheral Ca^{2+} release sites. Indeed, in the situation with 8-fold greater sarcolemmal Ca^{2+}

transport, activating 50% of the peripheral Ca^{2+} release sites caused only $\sim 20\%$ of the central Ca^{2+} release sites to respond. These data indicate that the sarcolemmal Ca^{2+} flux rate substantially influences the generation of Ca^{2+} signals within the centre of atrial myocytes. With greater sarcolemmal Ca^{2+} flux, a bigger initial trigger Ca^{2+} signal is needed to evoke a centripetal Ca^{2+} wave that reached and activated the central release sites. In essence, the sarcolemma acts to rapidly dampen the peripheral Ca^{2+} signals. The dampening prevents the wave guide activity described above, and also lessens the availability of Ca^{2+} that can cross the gap in RyR expression to initiate a centripetal Ca^{2+} wave.

We considered that SERCA pumps would similarly affect centripetal Ca^{2+} wave movement. However, the effect of changing SERCA activity (Fig. 6B) was more striking than that observed with sarcolemmal Ca^{2+} flux. To explore the consequences of altering SERCA activity, we used the same approach as described above for sarcolemmal Ca^{2+} flux; Ca^{2+} signals were triggered by activating a fraction of the peripheral Ca^{2+} release sites, and we monitored the subsequent recruitment of central Ca^{2+} release sites. As shown in Fig. 6B, varying τ, the SERCA pump strength, shifted the relationship between the trigger Ca^{2+} signal and the recruitment of central Ca^{2+} release sites. With relatively strong SERCA activity (red line in Fig. 6B), central Ca^{2+} release required activation of 80% of the peripheral Ca^{2+} release sites. As the SERCA activity was reduced, lesser fractions of the peripheral Ca^{2+} release sites were required to initiate recruitment of central Ca^{2+} release (black and blue lines in Fig. 6B). Moreover, as SERCA activity was reduced, we observed that even modest activation of peripheral Ca^{2+} release sites consistently evoked central responses. For example, the blue line in Fig. 6B illustrates that with the least SERCA activity examined, activation of 20% of peripheral Ca^{2+} release sites caused recruitment of $> 60\%$ of the central release sites. These data indicate that relatively weak initial triggers can be effective in causing propagation of Ca^{2+} waves if the SERCA activity is reduced.

Our data illustrate that both sarcolemmal Ca^{2+} flux and SERCA activity control the inward propagation of Ca^{2+} waves in atrial myocytes. But, SERCA activity has the most profound effect, and when its activity declines Ca^{2+} waves are initiated by relatively low amplitude trigger signals. The difference in the effectiveness of sarcolemmal Ca^{2+} flux versus SERCA relates to their relative position. Sarcolemmal Ca^{2+} flux predominantly affects peripheral Ca^{2+} signals, whereas SERCA pumps, which are expressed throughout a myocyte's volume, play a stronger role in dampening Ca^{2+} signal propagation.

Irregular arrangements of Ca^{2+} release sites

A regular arrangement of Ca^{2+} release sites is a critical feature of healthy striated muscle cells. However, under pathological conditions this regularity can be severely disrupted. The impact of an irregular expression of Ca^{2+} release sites on Ca^{2+} wave propagation can be readily studied within the simulation framework presented here. To achieve this, we silenced 75% of the Ca^{2+} release sites, using a randomised selection, and then initiated Ca^{2+} signals by activating peripheral Ca^{2+} release sites at the edge of the central z-disk (as shown in Fig. 3). The space-time plots in Figs. 7A – C show some of the different outcomes that can be observed following the random silencing of Ca^{2+} release sites. Figure. 7A, for example, illustrates a situation in which Ca^{2+} release remained restricted around the plane of the initial trigger. The Ca^{2+} signal did not propagate appreciably, and Ca^{2+} release activity ceased completely after ~ 0.5 s. In contrast, Fig. 7B depicts the initiation of longitudinal Ca^{2+} waves that travelled towards the top and bottom of the cell. The Ca^{2+} wave successfully reached the bottom of the cell, but faltered before reaching the top. A similar bi-directional Ca^{2+} wave is illustrated in Fig. 7C, but in this case the Ca^{2+} waves did manage to reach both the top and bottom of the cell, but took longer to do so and initiated short-lived, at times back-propagating, mini-waves as they travelled. These data indicate that randomising the distribution of active Ca^{2+} release sites gives rise to less robust, and substantially heterogeneous, responses. This is most likely due to variations in the distances over which Ca^{2+} ions have to diffuse in order to maintain a regenerative Ca^{2+} wave via CICR. The heterogeneity of Ca^{2+} wave propagation caused by randomising the positions of active Ca^{2+} release sites can be overcome by increasing the release strength (Figs. 7D and E). Using the same conditions of 75% silenced Ca^{2+} release sites as in Figs. 7A–C, but with release strength increased to 15 μM μm^3/s (Fig. 7D) or 25 μM μm^3/s (Fig. 7E) it is evident that Ca^{2+} waves propagate with progressively greater fidelity and less heterogeneity. Moreover, the Ca^{2+} waves propagate more rapidly through the cell volume as the release strength increases. The fidelity of Ca^{2+} wave initiation and propagation is also affected by the proportion of Ca^{2+} release sites that are active. Figs. 7F and G show Ca^{2+} waves in simulations where the fraction of silenced release sites was 65% (Fig. 7F) and 55% (Fig. 7G). Compared to the situations with 75% of the release sites being silenced (Figs. 7A – C), Ca^{2+} waves clearly occur with greater fidelity, velocity and amplitude if there are more functional Ca^{2+} release sites. These data indicate that small changes in the distribution of Ca^{2+} release sites or release strength can profoundly
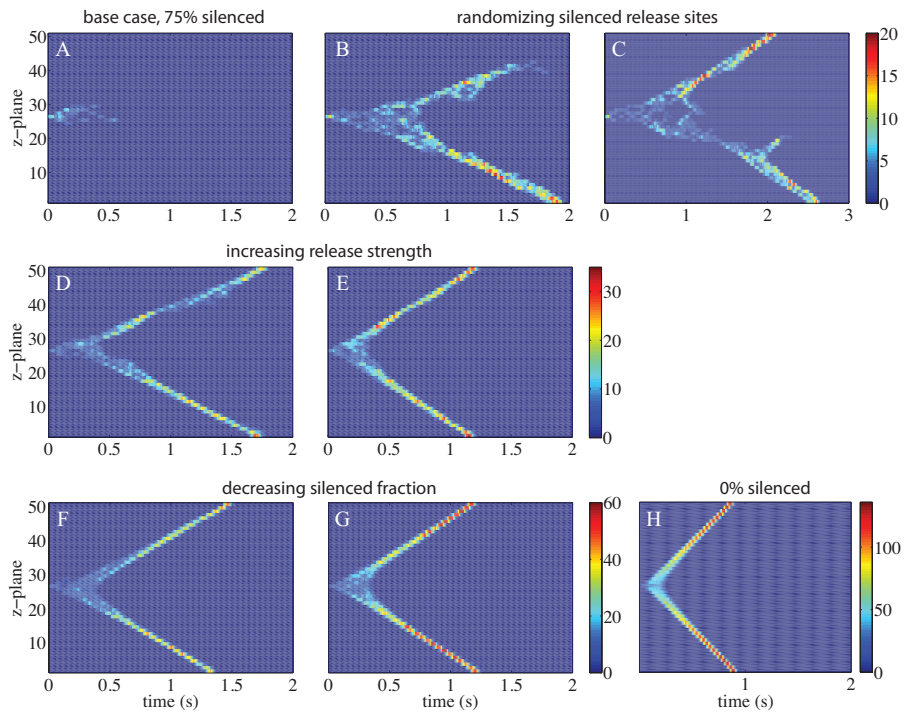
Figure 7: Ca^{2+} release activity when Ca^{2+} release sites are randomly silenced. (A) Base case when 75% of release sites are randomly silenced. Parameter values are $\tau = 0.4$ s, $t_{\mathrm{ref}} = 1.3$ s, $\sigma = 13\mu$M μm^3/s. The parameter values for (B)–(G) are identical to those in (A), but different positions of silenced release sites (B,C), $\sigma = 15\mu$M μm^3/s (D), $\sigma = 25\mu$M μm^3/s (E), silenced fraction is 65% (F), 55% (G) and 0% (H). Colours represent the number of Ca^{2+} liberating release sites in a single z-disk and correspond to the values shown on the colour bar to the right. Other parameter values as in Table 1.

influence the shape and movement of intracellular Ca^{2+} waves.

Stochastic Ca^{2+} release

So far, we have only considered outcomes where the threshold for CICR at all Ca^{2+} release sites was set at a particular value. However, it is known from both experimental and theoretical studies that the activation of intracellular Ca^{2+} release channels is intrinsically stochastic (16, 50–54). This stochasticity mainly arises from the random state transitions of Ca^{2+}-releasing channels, thereby giving rise to an unpredictable onset of Ca^{2+} liberation. For the next series of simulations we did not employ a constant threshold for CICR, but rather mimicked stochastic activity by introducing randomness into the threshold for activating Ca^{2+} channels. Our framework is ideally suited for this purpose because it is relatively simple to replace the term for a constant CICR threshold with one that generates stochastic thresholds with a pre-determined variability (see Eq. (13) in Materials and Methods). In essence, each Ca^{2+} release site within the model is given a random threshold for activation. The variability of thresholds is independently controlled.

The consequence of random CICR thresholds on Ca^{2+} wave propagation is illustrated in Fig. 8. This figure depicts Ca^{2+} waves with the same initiation conditions (activation of a few Ca^{2+} release sites in the central z-disk), distribution of active Ca^{2+} release sites and parameter values as Fig. 7B, but with different degrees of randomness for the CICR thresholds at each Ca^{2+} release site. With a relatively small degree of randomness (Fig. 8A) Ca^{2+} waves look almost identical to that in the previous deterministic simulations (cf. Figs. 7B and 8A); there is some successful, and some faltering, propagation of the Ca^{2+} wave to the top and bottom of the cell.

We next explored the effect of having more random CICR thresholds on Ca^{2+} wave propagation. We did this by progressively increasing the variability of CICR thresholds at each Ca^{2+} release site. It could be considered that increasing the variability for activation of Ca^{2+} release might stifle Ca^{2+} wave propagation. This could plausibly happen due to mis-matching of CICR thresholds between neighbouring Ca^{2+} release sites. However, we found the opposite to be true. Increasing the variability of random CICR thresholds produced Ca^{2+} waves with more robust propagation (Figs. 8A through 8D). These data imply that variable CICR thresholds have a constructive role in intracellular Ca^{2+} signalling.

In addition to promoting the successful propagation of Ca^{2+} waves, increasing the variability of CICR thresholds had another progressively emergent effect; i.e. the triggering of spontaneous Ca^{2+} signals. For example,
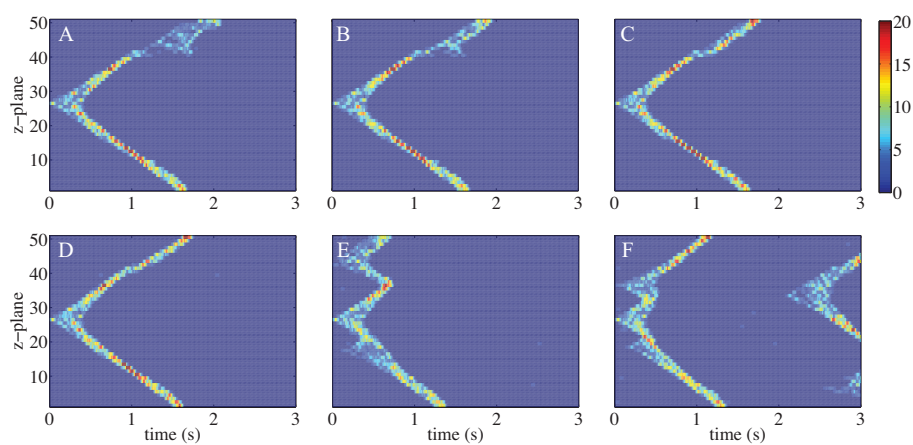
Figure 8: Stochastic Ca^{2+} waves for the same initial condition, distribution of silenced Ca^{2+} release sites and parameter values as in Fig. 7B for $\beta = 200$ μM^{-1} (A), 150 μM^{-1} (B), 100 μM^{-1} (C), 90 μM^{-1} (D), 80 μM^{-1} (E) and 70 μM^{-1} (F). Colours represent the number of active Ca^{2+} release sites in a single z-disk and correspond to the values shown on the colour bar to the right.

Fig. 8E shows a situation in which a Ca^{2+} wave was triggered by activating a few Ca^{2+} release sites in the central z-disk (as in Figs. 8A – D), but simultaneous with this deliberately-triggered Ca^{2+} wave, two spontaneous Ca^{2+} waves were also initiated. Increasing the variability of CICR thresholds even more leads to the generation of repetitive propagating Ca^{2+} waves (Fig. 8F). This occurs because with more variable CICR thresholds, it is likely that some Ca^{2+} release sites will be activated even at resting cytosolic Ca^{2+} concentrations. Eventually, increasing the variability of CICR thresholds leads to a complete breakdown in Ca^{2+} wave propagation, and causes the appearance of multiple, non-synchronous Ca^{2+} waves and non-propagating, subcellular Ca^{2+} events (Fig. 9). The panels in Fig. 9 show three independent
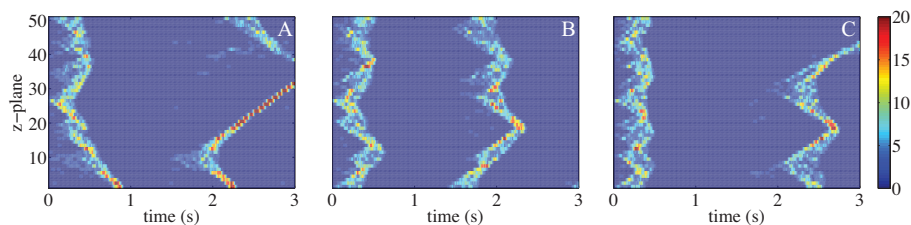

Figure 9: Stochastic Ca^{2+} waves for the same initial condition, distribution of silenced Ca^{2+} release sites and parameter values as in Fig. 7B for $\beta = 60 \ \mu M^{-1}$. The panels (A)–(C) illustrate the different patterns of spontaneous Ca^{2+} release observed with highly random thresholds for different realisations of the fluctuating threshold for Ca^{2+} release. Colours represent the number of active Ca^{2+} release sites in a single z-disk and correspond to the values shown on the colour bar to the right.

simulations using the same parameters and the same variability of CICR thresholds. Three results are presented to depict the variable responses that are observed when CICR thresholds exhibit significant variability. In this situation, the variability of thresholds is so large that multiple Ca^{2+} release sites will be activated by the resting cytosolic Ca^{2+} concentration. Under these conditions, it is likely that an atrial myocyte would be highly arrhythmic.

Conclusion

The studies presented here highlight the need for three-dimensional cellular models to faithfully capture the complex spatio-temporal patterns of

intracellular Ca^{2+} signal propagation. Recent experiments demonstrate that changes in the spatial pattern of atrial myocyte Ca^{2+} signals occur in pathological conditions such as tachycardia (55). Our simulations illustrate that subtle changes in stimulation or cellular parameters can have significant, non-intuitive effects on Ca^{2+} signal initiation and propagation. Whilst current high-resolution imaging technologies can achieve millisecond frame rates, such speeds are generally only possible with a static image plane. As a consequence, Ca^{2+} movement outside the plane of focus is not observed. Since it is impossible *a priori* to know the location of Ca^{2+} release activity, imaging studies that are limited to a subcellular plane are likely to underestimate the occurrence of subtle changes in Ca^{2+} signal initiation and propagation. In the context of atrial myocytes, we have previously demonstrated that a pro-arrhythmic, self-sustaining Ca^{2+} wave (denoted a 'ping wave'; (20)) can originate within a single z-disk due to the activation of only a few Ca^{2+} release sites. The rotational propagation of ping waves within a z-disk is unlikely to be detected using imaging because atrial myocytes are conventionally imaged lying on their side, and not on an end. Moreover, the observations of enhanced Ca^{2+} ion diffusion by wave guiding (Figs. 3 and 4), and longitudinal Ca^{2+} waves evoked by ping waves (20), serve to illustrate that the true impact of Ca^{2+} signals is only revealed in three dimensions.

While the computational framework presented here is inspired by, and tailored to, the dynamics of intracellular Ca^{2+} transport in atrial myocytes, the main concepts may be applicable to other cell types. The notion of Ca^{2+} excitability of the RyR underpins the use of threshold models for Ca^{2+} liberation from the SR. However, Ca^{2+} excitability is not an exclusive feature of the RyR, as the $InsP_3R$ exhibits the same phenomenon (14, 56). CICR is the key mechanism underlying saltatory Ca^{2+} waves arising from either RyRs or $InsP_3Rs$. In both cases, Ca^{2+} waves rely on the successive activation of clusters of channels (8). These commonalities between RyR- and $InsP_3R$-driven Ca^{2+} transport render the current simulation technique a promising candidate for studying Ca^{2+} dynamics in non-excitable cells, such as oocytes and hepatocytes, where Ca^{2+} is liberated from the ER through $InsP_3Rs$. Ca^{2+} signalling in non-excitable cells is much slower than in excitable cells. Typically, non-excitable cell types show Ca^{2+} oscillations with periods of tens of seconds or longer (5, 6). In comparison Ca^{2+} signals in excitable cells such as atrial myocytes can arise within tens of milliseconds. Importantly our modelling approach can handle both fast and slow Ca^{2+} signals. Most cell types (e.g. neurons and non-excitable cells) have less regular distributions of Ca^{2+} release sites when compared to atrial myocytes (57). The efficiency of the modelling framework presented here does

not rely on the regular arrangement of RyRs in atrial myocytes, but can equally well describe random distributions of Ca^{2+} release sites such as in a hepatocyte. Indeed our results in Fig. 7 could be interpreted as hormone-evoked Ca^{2+} waves originating from a subcellular region in hepatocytes (58). The subcellular initiation of Ca^{2+} signals in this case could reflect the local production of $InsP_3$, and the Ca^{2+} release sites would represent clusters of $InsP_3Rs$. The adaptation of the modelling ideas outlined here requires two main steps. Firstly, the derivation and implementation of the Green's function that is commensurate with the cell type under investigation is needed. The former becomes necessary and is non-trivial when the cell shape differs from regular geometries such as cubes, cuboids, spheres and cylinders for which the Green's functions are documented. The latter poses a significant computational challenge when working at high spatial resolution and active signalling sites close to the cell boundary. Secondly, the new threshold model needs to reproduce key experimental findings for the cell type of interest. Implementing cell-specific expression patterns of Ca^{2+} channels, pumps and buffers in a particular cellular morphology does not guarantee *a priori* a physiologically realistic model. Once these two steps have been accomplished the resultant model is a powerful resource that allows for quick scans of physiologically relevant parameters to aid in the design of future experiments and that provides valuable insights into the complex interactions of Ca^{2+} microdomains across the entire cellular volume that generate measurable whole-cell responses.

References

[1] Berridge, M. J., P. Lipp, and M. D. Bootman, 2000. The versatility and universality of calcium signalling. *Nature Reviews Molecular Cell Biology* 1:11–21.

[2] Berridge, M. J., 2006. Calcium microdomains: organization and function. *Cell Calcium* 40:405–412.

[3] Bootman, M. D., M. J. Berridge, and H. Roderick, 2002. Calcium Signalling: More Messengers, More Channels, More Complexity. *Current Biology* 12:R563–R565.

[4] Bers, D. M., 2002. Cardiac excitation-contraction coupling. *Nature* 415:198–205.

[5] Berridge, M. J., and A. Galione, 1988. Cytosolic Calcium Oscillators. *The FASEB Journal* 2:3074–3082.

[6] Thul, R., T. C. Bellamy, H. L. Roderick, M. D. Bootman, and S. Coombes, 2008. Calcium oscillations. *Advances in Experimental Medicine and Biology* 641:1–27.

[7] Bartlett, P. J., L. D. Gaspers, N. Pierobon, and J. Thomas, 2014. Calcium-dependent regulation of glucose homeostasis in the liver. *Cell Calcium* in press.

[8] Roderick, H. L., M. J. Berridge, and M. D. Bootman, 2003. Calcium-induced calcium release. *Current Biology* 13:R425.

[9] Mackenzie, L., M. D. Bootman, M. J. Berridge, and P. Lipp, 2001. Predetermined recruitment of calcium release sites underlies excitation-contraction coupling in rat atrial myocytes. *The Journal of Physiology* 530:417–429.

[10] Blatter, L. A., J. Kockskämper, K. A. Sheehan, A. V. Zima, J. Hüser, and S. L. Lipsius, 2003. Local calcium gradients during excitation-contraction coupling and alternans in atrial myocytes. *The Journal of Physiology* 546:19–31.

[11] Bootman, M. D., I. Smyrnias, R. Thul, S. Coombes, and H. L. Roderick, 2011. Atrial cardiomyocyte calcium signalling. *Biochimica et Biophysica Acta* 1813:922–934.

[12] Bootman, M. D., D. Harzheim, I. Smyrnias, S. J. Conway, and H. L. Roderick, 2007. Temporal changes in atrial EC-coupling during prolonged stimulation with endothelin-1. *Cell Calcium* 42:489–501.

[13] Ito, J. J., J. J. Parrington, and R. A. R. Fissore, 2011. PLCζ and its role as a trigger of development in vertebrates. *Molecular Reproduction and Development* 78:846–853.

[14] Bezprozvanny, I., 2013. Bilayer measurement of endoplasmic reticulum Ca^{2+} channels. *Cold Spring Harbour Protocols* 2013:pdb.top066225.

[15] Bootman, M., E. Niggli, M. Berridge, and P. Lipp, 1997. Imaging the hierarchical Ca^{2+} signalling system in HeLa cells. *The Journal of Physiology* 499 (Pt 2):307–314.

[16] Marchant, J., N. Callamaras, and I. Parker, 1999. Initiation of IP$_3$-mediated Ca^{2+} waves in Xenopus oocytes. *Embo Journal* 18:5285–5299.

[17] Thul, R., S. Coombes, H. L. Roderick, and M. D. Bootman, 2012. Sub-cellular calcium dynamics in a whole-cell model of an atrial myocyte. *Proceedings of the National Academy of Sciences of the United States of America* 109:2150–2155.

[18] Mackenzie, L., H. L. Roderick, M. J. Berridge, S. J. Conway, and M. D. Bootman, 2004. The spatial pattern of atrial cardiomyocyte calcium signalling modulates contraction. *Journal of Cell Science* 117:6327–6337.

[19] Chen-Izu, Y., S. L. McCulle, C. W. Ward, C. Soeller, B. M. Allen, C. Rabang, M. B. Cannell, C. W. Balke, and L. T. Izu, 2006. Three-dimensional distribution of ryanodine receptor clusters in cardiac myocytes. *Biophysical Journal* 91:1–13.

[20] Thul, R., S. Coombes, and M. D. Bootman, 2012. Persistence of pro-arrhythmic spatio-temporal calcium patterns in atrial myocytes: a computational study of ping waves. *Frontiers in Physiology* 3:279.

[21] Sneyd, J., and K. Tsaneva-Atanasova, 2002. Modeling Calcium Waves. *In* M. Falcke, and D. Malchow, editors, Understanding Calcium Dynamics, Springer, 179–199.

[22] Falcke, M., 2004. Reading the patterns in living cells - the physics of Ca^{2+} signaling. *Advances in Physics* 53:255–440.

[23] Thurley, K., A. Skupin, R. Thul, and M. Falcke, 2012. Fundamental properties of Ca^{2+} signals. *Biochimica et Biophysica Acta* 1820:1185–1194.

[24] Dupont, G., L. Combettes, G. S. Bird, and J. W. Putney, 2011. Calcium oscillations. *Cold Spring Harbor Perspectives in Biology* 3:pii: a004226.

[25] Dupont, G., and H. Croisier, 2010. Spatiotemporal organization of Ca^{2+} dynamics: a modeling-based approach. *HFSP Journal* 4:43–51.

[26] Dupont, G., 2014. Modeling the intracellular organization of calcium signaling. *Wiley Interdisciplinary Reviews. Systems Biology and Medicine* 6:227–237.

[27] Shannon, T. R., F. Wang, J. Puglisi, C. Weber, and D. M. Bers, 2004. A mathematical treatment of integrated Ca^{2+} dynamics within the ventricular myocyte. *Biophysical Journal* 87:3351–3371.

[28] Thul, R., G. D. Smith, and S. Coombes, 2008. A bidomain threshold model of propagating calcium waves. *Journal of Mathematical Biology* 56:435–463.

[29] Coombes, S., 2001. The effect of ion pumps on the speed of travelling waves in the fire-diffuse-fire model of Ca^{2+} release. *Bulletin of Mathematical Biology* 63:1–20.

[30] Skupin, A., H. Kettenmann, and M. Falcke, 2010. Calcium signals driven by single channel noise. *PLoS Computational Biology* 6:e1000870.

[31] Thurley, K., and M. Falcke, 2011. Derivation of Ca^{2+} signals from puff properties reveals that pathway function is robust against cell variability but sensitive for control. *Proceedings of the National Academy of Sciences of the United States of America* 108:427–432.

[32] Thul, R., S. Coombes, and G. D. Smith, 2009. Sensitisation waves in a bidomain fire-diffuse-fire model of intracellular Ca^{2+} dynamics. *Physica D: Nonlinear Phenomena* 238:2142–2152.

[33] Barton, G., 2005. Elements of Green's Functions and Propagation: Potentials, Diffusion, and Waves. Clarendon Press, Oxford.

[34] Abramowitz, M., and I. Stegun, 1974. Handbook of mathematical functions. Dover Publications, New York.

[35] Capoen, W., J. Sun, D. Wysham, M. S. Otegui, M. Venkateshwaran, S. Hirsch, H. Miwa, J. A. Downie, R. J. Morris, J.-M. Ané, and G. E. D. Oldroyd, 2011. Nuclear membranes control symbiotic calcium signaling of legumes. *Proceedings of the National Academy of Sciences of the United States of America* 108:14348–14353.

[36] Hille, B., 2002. Ion Channels of Excitable Membranes. Sinauer Associates, Sunderland, third edition edition.

[37] Keener, J. P., 2006. Stochastic calcium oscillations. *Mathematical Medicine and Biology* 23:1–25.

[38] Keener, J. P., 2009. Invariant manifold reductions for Markovian ion channel dynamics. *Journal of Mathematical Biology* 58:447–457.

[39] Williams, G. S. B., M. A. Huertas, E. A. Sobie, M. S. Jafri, and G. D. Smith, 2007. A probability density approach to modeling local control of calcium-induced calcium release in cardiac myocytes. *Biophysical Journal* 92:2311–2328.

[40] DeRemigio, H., M. D. LaMar, P. Kemper, and G. D. Smith, 2008. Markov chain models of coupled calcium channels: Kronecker representations and iterative solution methods. *Physical Biology* 5.

[41] Nguyen, V., R. Mathias, and G. D. Smith, 2005. A stochastic automata network descriptor for Markov chain models of instantaneously coupled intracellular Ca^{2+} channels. *Bulletin of Mathematical Biology* 67:393–432.

[42] Coombes, S., and Y. Timofeeva, 2003. Sparks and waves in a stochastic fire-diffuse-fire model of Ca^{2+} release. *Physical Review E* 68:021915.

[43] Soeller, C., and D. Baddeley, 2013. Super-resolution imaging of EC coupling protein distribution in the heart. *Journal of Molecular and Cellular Cardiology* 58:32–40.

[44] Baddeley, D., I. D. Jayasinghe, L. Lam, S. Rossberger, M. B. Cannell, and C. Soeller, 2009. Optical single-channel resolution imaging of the ryanodine receptor distribution in rat cardiac myocytes. *Proceedings of the National Academy of Sciences of the United States of America* 106:22275–22280.

[45] Granqvist, E., D. Wysham, S. Hazledine, W. Kozlowski, J. Sun, M. Charpentier, T. V. Martins, P. Haleux, K. Tsaneva-Atanasova, J. A. Downie, G. E. D. Oldroyd, and R. J. Morris, 2012. Buffering capacity explains signal variation in symbiotic calcium oscillations. *Plant Physiology* 160:2300–2310.

[46] Song, L.-S., S. Guatimosim, L. Gómez-Viquez, E. A. Sobie, A. Ziman, H. Hartmann, and W. J. Lederer, 2005. Calcium biology of the transverse tubules in heart. *Annals of the New York Academy of Sciences* 1047:99–111.

[47] Richards, M. A., J. D. Clarke, P. Saravanan, N. Voigt, D. Dobrev, D. A. Eisner, A. W. Trafford, and K. M. Dibb, 2011. Transverse tubules are

a common feature in large mammalian atrial myocytes including human. *American Journal of Physiology. Heart and Circulatory Physiology* 301:H1996–2005.

[48] Smyrnias, I., W. Mair, D. Harzheim, S. A. Walker, H. L. Roderick, and M. D. Bootman, 2010. Comparison of the T-tubule system in adult rat ventricular and atrial myocytes, and its role in excitation-contraction coupling and inotropic stimulation. *Cell Calcium* 47:210–223.

[49] Carl, S., K. Felix, A. Caswell, N. Brandt, W. Ball, P. Vaghy, G. Meissner, and D. Ferguson, 1995. Immunolocalization of Sarcolemmal Dihydropyridine Receptor and Sarcoplasmic Reticular Triadin and Ryanodine Receptor in Rabbit Ventricle and Atrium. *The Journal of Cell Biology* 129:673–682.

[50] Falcke, M., 2003. On the role of stochastic channel behavior in intracellular Ca^{2+} dynamics. *Biophysical Journal* 84:42–56.

[51] Thul, R., and M. Falcke, 2004. Stability of membrane bound reactions. *Physical Review Letters* 93:188103.

[52] DeRemigio, H., and G. D. Smith, 2005. The dynamics of stochastic attrition viewed as an absorption time on a terminating Markov chain. *Cell Calcium* 38:73–86.

[53] Dupont, G., A. Abou-Lovergne, and L. Combettes, 2008. Stochastic aspects of oscillatory Ca^{2+} dynamics in hepatocytes. *Biophysical Journal* 95:2193–2202.

[54] Dickinson, G. D., and I. Parker, 2013. Factors Determining the Recruitment of Inositol Trisphosphate Receptor Channels During Calcium Puffs. *Biophysical Journal* 105:2474–2484.

[55] Greiser, M., B.-G. Kerfant, G. S. B. Williams, N. Voigt, E. Harks, K. M. Dibb, A. Giese, J. Meszaros, S. Verheule, U. Ravens, M. A. Allessie, J. S. Gammie, J. van der Velden, W. J. Lederer, D. Dobrev, and U. Schotten, 2014. Tachycardia-induced silencing of subcellular Ca^{2+} signaling in atrial myocytes. *The Journal of Clinical Investigation* 124:4759–4772.

[56] Foskett, J. K., C. White, K.-H. Cheung, and D.-O. D. Mak, 2007. Inositol trisphosphate receptor Ca^{2+} release channels. *Physiological Reviews* 87:593–658.

[57] Tovey, S. C., P. de Smet, P. Lipp, D. Thomas, K. W. Young, L. Missi-aen, H. De Smedt, J. B. Parys, M. J. Berridge, J. Thuring, A. Holmes, and M. D. Bootman, 2001. Calcium puffs are generic InsP$_3$-activated elementary calcium signals and are downregulated by prolonged hormonal stimulation to inhibit cellular calcium responses. *Journal of Cell Science* 114:3979–3989.

[58] Rooney, T. A., E. J. Sass, and A. P. Thomas, 1990. Agonist-Induced Cytosolic Calcium Oscillations Originate From a Specific Locus in Single Hepatocytes. *The Journal of Biological Chemistry* 265:10792–10796.

[59] Cohen, H., F. Rodriguez Villegas, and D. Zagier, 2000. Convergence acceleration of alternating series. *Experimental Mathematics* 9:3–12.

[60] van Wijngaarden, A., 1965. *Cursus Wetenschappelijk Rekenen B: Process Analyse*. Technical report, Stichting Mathematisch Centrum.

Appendix

In this section, we provide further details on the practical numerical evaluation of Eq. 6. A key step in the computation of the Ca^{2+} concentration is the evaluation of the basis function $H\left(\mathbf{r}, \mathbf{r}', dt\right)$, which can be written as

$$H\left(\mathbf{r}, \mathbf{r}', dt\right) = \sum_{n=-\infty}^{\infty} \sum_{\alpha,\beta} P_\alpha(z, z') Q_{n,\beta}(r, \theta, r', \theta') \int_0^{dt} p_\alpha(s) q_\beta(s) ds. \quad \text{(A.1)}$$

Since P and Q are already known from the calculation of the Green's function, we only need to evaluate the integral

$$I = \int_0^{dt} e^{-(e+f)s} ds = \frac{1 - e^{-(e+f)dt}}{e + f}, \quad \text{(A.2)}$$

with $e = D\beta^2$ and $f = D\alpha^2 + 1/\tau$. Due to the denominator, Eq. A.2 does not readily factorise into two functions depending only on α and β, respectively, as in the expression for G (see Eqs. 10). However, this factorisation proves to be crucial for fast calculation. In the following, we describe a transformation that achieves such a factorisation and then demonstrate an efficient scheme for its computation. Starting from the representation of Dirac's delta function (33)

$$\delta(u - s) = \frac{2}{dt} \sum_{n=1}^{\infty} \sin\left(\frac{n\pi u}{dt}\right) \sin\left(\frac{n\pi s}{dt}\right), \quad \text{(A.3)}$$

for $u, s \in [0, dt]$, we find

$$\begin{aligned}
I &= \int_0^{dt} du \int_0^{dt} ds\, e^{-es - fu} \delta(u - s) \\
&= \frac{2}{dt} \sum_{n=1}^{\infty} \int_0^{dt} e^{-es} \sin\left(\frac{n\pi s}{dt}\right) ds \int_0^{dt} e^{-fu} \sin\left(\frac{n\pi u}{dt}\right) du,
\end{aligned} \quad \text{(A.4)}$$

which yields

$$I = \frac{2}{dt} \left[e^{-(e+f)dt} + 1\right] E(e, f) - \frac{2}{dt} \left[e^{-edt} + e^{-fdt}\right] F(e, f), \quad \text{(A.5)}$$

with

$$E(e, f) = \sum_{n=1}^{\infty} \left(\frac{n\pi}{\mathrm{d}t}\right)^2 \left\{ \left[e^2 + \left(\frac{n\pi}{\mathrm{d}t}\right)^2\right] \left[f^2 + \left(\frac{n\pi}{\mathrm{d}t}\right)^2\right] \right\}^{-1}, \qquad \text{(A.6a)}$$

$$F(e, f) = \sum_{n=1}^{\infty} (-1)^n \left(\frac{n\pi}{\mathrm{d}t}\right)^2 \left\{ \left[e^2 + \left(\frac{n\pi}{\mathrm{d}t}\right)^2\right] \left[f^2 + \left(\frac{n\pi}{\mathrm{d}t}\right)^2\right] \right\}^{-1}. \quad \text{(A.6b)}$$

It is evident from Eq. A.6 that all terms depending on e are now multiplied by terms that depend on f only. The introduction of infinite sums instead of a closed expression as in Eq. A.2 may appear as a step back because now we need to consider the quality of convergence. Indeed, these series converge very slowly for large values of e and f, which prohibits a straight forward implementation of Eqs. A.6.

However, powerful tools for convergence acceleration of alternating series exist (59). In summary, they correspond to a resummation of the original series such that the relative accuracy of the first n terms scales like γ^{-n} for some constant $\gamma > 1$. As it turns out, Eq. A.6b satisfies all necessary conditions, so that we can apply this algorithm. To do the same with Eq. A.6a, we first need to transform it into an alternating series. Given that all terms of E are positive, we follow van Wijngaarden (60). Let b_k denote the terms of the original series, then

$$\sum_{k=0}^{\infty} b_k = \sum_{k=0}^{\infty} (-1)^k a_k, \qquad \text{(A.7)}$$

with

$$a_k = \sum_{j=0}^{\infty} 2^j b_{2^j(k+1)-1} = b_k + 2b_{2k+1} + 4b_{4k+3} + \dots . \qquad \text{(A.8)}$$

A fast computation of the time integral in Eq. 5 requires us to evaluate two infinite sums. Figure 10 shows the quality of the algorithm as described above that we use for this task. There is almost no difference between the exact value and the approximation, with a relative error smaller than 10^{-3} for almost all arguments. The range of β corresponds to the one used in the simulations. Note that the value of α spans 4 orders of magnitude without affecting the convergence accuracy. A comparison between the infinite sums and their approximations is facilitated by knowing E and F in closed form
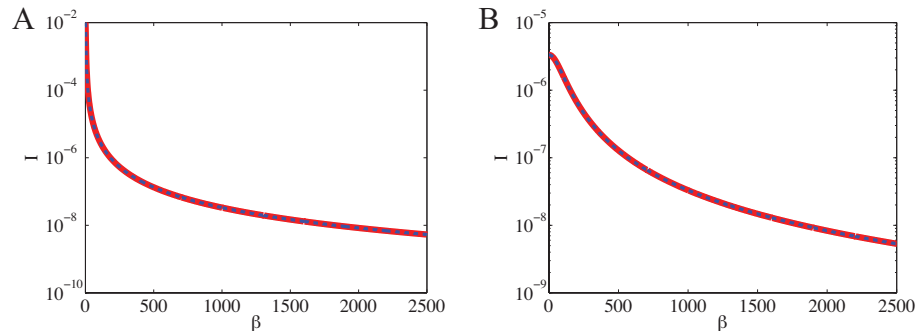
Figure 10: Exact value of the time integral (solid red line) and the factorised approximation (blue dashed line) for $\alpha = 0.01$ m^{-1} (A) and $\alpha = 100$ m^{-1} (B). We use only the 3 leading terms for the convergence acceleration and the leading 15 terms to compute a_k in Eq. A.8. Parameter values as in Table 1 .

due to

$$\sum_{n=0}^{\infty} \frac{n^2}{(n^2 + e^2)(n^2 + f^2)} = \pi \frac{e \coth(\pi e) - f \coth(\pi f)}{2(e^2 - f^2)} , \tag{A.9a}$$

$$\sum_{n=0}^{\infty} \frac{(-1)^n \, n^2}{(n^2 + e^2)(n^2 + f^2)} = \pi \frac{e \sinh(\pi f) - f \sinh(\pi e)}{2(e^2 - f^2) \sinh(\pi e) \sinh(\pi f)} . \tag{A.9b}$$

Parameter	Value	Unit
Height of cylinder l	100.6	μm
Radius of cylinder R	6	μm
Radial flux strength h	0.01	s^{-1}
Flux strength at $z = 0$ h_0	0.0120	s^{-1}
Flux strength at $z = l$ h_l	0.0135	s^{-1}
Diffusion coefficient of Ca^{2+} D	30	μm^{2}s^{-1}
Pump strength τ	0.4	s
Release time t_{rel}	0.05	s
Refractory time t_{ref}	0.5	s
Threshold Ca^{2+} concentration c_{th}	0.15	μM
Number of Bessel functions in Green's function $m_{\max}^{GF}$	3000	
Number of radial modes in Green's function $\beta_{\max}^{GF}$	3000	
Number of axial modes in Green's function $\alpha_{\max}^{GF}$	5000	
Number of Bessel functions in time integral $m_{\max}^{TI}$	2100	
Number of radial modes in time integral $\beta_{\max}^{TI}$	600	
Number of axial modes in time integral $\alpha_{\max}^{TI}$	4000	
Radial discretisation dr	0.1	μm
Angular discretisation dθ	0.0838	
Axial discretisation dz	0.1	μm
Temproal discretisation dt	0.01	s

Table 1: Default parameter values